

Applications of High-resolution High-precision Spectral Observations in Solar Physics

Hao Ran

July 23, 2024

Contents

1	Introduction	2
2	High-resolution Spectral Observations of the Sun	2
2.1	Methods	2
2.1.1	Application of the Zeeman Effects	2
2.1.2	Doppler Velocity Measurements	4
2.1.3	Profile Analysis	5
2.2	Typical Wavebands and Their Research Significance	5
2.2.1	Photosphere	5
2.2.2	Chromosphere and Transition Region	7
2.2.3	Corona	12
3	Some Existing Solar Observatories and Their Performance	12
3.1	New Vacuum Solar Telescope (NVST)	12
3.2	GREGOR Solar Telescope	12
3.3	Solar Dynamics Observatory (SDO)	12

1 Introduction

With but few exceptions, quantitatively researches of the Sun are based on the interpretation of spectroscopic observations. Whether such data are collected at radio, visual, or X-ray wavelengths, their interpretation rest upon our ability. First, to identify the process by which the radiation is produced, second, to interpret the radiation in terms of local plasma conditions at the place of origin, and third, to organize the different plasma regimes observed at different wavelengths in proper relationship (Zirin 1988 [18]).

To illustrate the problems involved in each of these steps, we consider a spectrum giving specific intensity I_λ as a function of wavelength. We represent the functional dependence of the spectrum in the symbolic form:

$$I_\lambda(r_i, S_i, \varphi_{\lambda i}, \kappa_{0i}, \Delta z_i, \Delta\lambda, \Delta\theta, \Delta t),$$

where r_i denotes the different radiation processes (such as line and continuum), S_i denotes the source function for photons of species i , $\varphi_{\lambda i}$ denotes the absorption profile, κ_{0i} is the absorption coefficient, Δz_i denotes the spread in the line-of-sight distance within which the observed radiation originates, $\Delta\lambda$, $\Delta\theta$, and Δt denote the spectral, spatial, and temporal resolution, respectively. Note that the latter three quantities are determined by the instrument. The first five quantities are, on the other hand, determined by the solar atmosphere, and convey the most of informations about the atmosphere (Sturrock et al. 2013 [13]).

2 High-resolution Spectral Observations of the Sun

2.1 Methods

2.1.1 Application of the Zeeman Effects

The Zeeman effect refers to the splitting of spectral lines due to the presence of an external magnetic field. Figure 1 shows a typical example of a spectral line observed of the sunspot is split into three components under the influence of the photosphere magnetic field, which clearly shows the Zeeman effect. In the absence of an external magnetic field, emission is observed as a single spectral line and is dependent only on the *principle quantum number* of the initial and final states. With the existence of a magnetic field, the principle number of each state is split into several substates, resulting in permitted transitions that have frequencies above the below the original frequency. The number of split levels is given by $(2 \times L + 1)$, where L is the *orbital angular momentum quantum number*. The degree of the splitting is proportional to the strength of the magnetic field. Note that not all transitions are allowed. The selection rule for the Zeeman effect is $\Delta m_l = 0, \pm 1$, where m_l is the *magnetic quantum number* (See Figure 2).

The Zeeman effect that occurs for spectral lines resulting from a transition between singlet states is called the *normal Zeeman effect*, while that which occurs when the total spin of either the initial or final states, or both, is nonzero is called the *anomalous Zeeman effect*. There is no fundamental difference between the two types. In the anomalous Zeeman effect, each energy is split into $2j + 1$ levels. The energy shift relative to the position of the non-splitting line is:

$$\Delta E = g m_j \frac{e \hbar B}{2 m_e} = g m_j \mu_B B,$$

here, g is the *Landé g-factor*, m_j is the *magnetic quantum number*, e is the *elementary charge*, \hbar is the *reduced Planck constant*, B is the *magnetic field strength*, m_e is the *electron mass*, and μ_B is the *Bohr magneton*. The Landé g-factor is given by:

$$g = 1 + \frac{j(j+1) + s(s+1) - l(l+1)}{2j(j+1)},$$

where j is the *total angular momentum quantum number*, s is the *spin quantum number*, and l is the *orbital angular momentum quantum number*. Note that for $s = 0$, $j = 1$, and $g = 1$, the above equation gives the splitting in the normal Zeeman effect.

Since that we have roughly understood the principle, we can now give an example of using the Zeeman effect to calculate the magnetic field of the Sun. Suppose that the sodium D_1 line (589.8

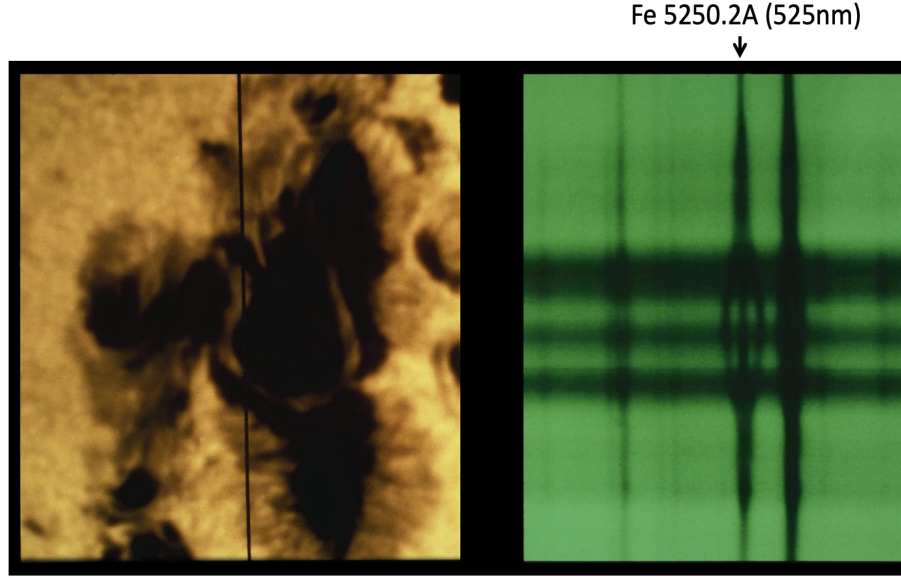


Figure 1: Observation of the Zeeman effect. The black vertical line on the white light image (left) shows the location of the slit for the spectrum which took the spectrum (right). The spectral line is split into three components, which clearly shows the Zeeman effect.

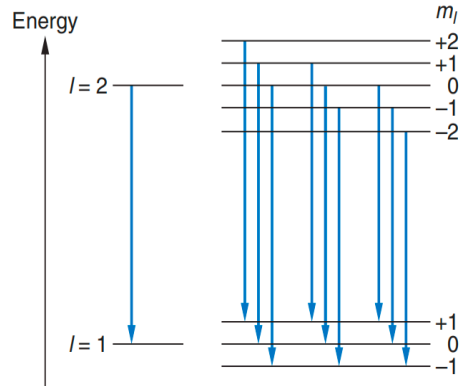


Figure 2: Energy-level splitting for singlet levels $l = 2$ and $l = 1$. Each level is split into $2l + 1$ terms. The rule $\Delta m_l = 0, \pm 1$ restricts the number of possible transitions to the nine shown.

nm) emitted in a particular region of the solar disk is observed to split into a four-component Zeeman effect. The wavelength difference $\Delta\lambda$ measured between the two outer components is 0.022 nm. What is the strength of the magnetic field in this region of the Sun?

The Sodium D_1 line is emitted by a transition from the $3^2P_{1/2}$ to $3^2S_{1/2}$. We can compute the ΔE values of each level as follows:

For the $3^2P_{1/2}$ level:

$$g = 1 + \frac{1/2(1/2 + 1) + 1/2(1/2 + 1) - 1(1 + 1)}{(2)(1/2)(1/2 + 1)} = 2/3,$$

the energy shift is:

$$\Delta E = (2/3)(\pm 1/2)(5.79 \times 10^{-9} \text{ eV/G})B.$$

For the $3^2S_{1/2}$ level:

$$g = 1 + \frac{1/2(1/2 + 1) + 1/2(1/2 + 1) - 1(1 + 1)}{(2)(1/2)(1/2 + 1)} = 2,$$

the energy shift is:

$$\Delta E = (2)(\pm 1/2)(5.79 \times 10^{-9} \text{ eV/G})B.$$

The longest-wavelength line ($m_j = -1/2 \rightarrow +1/2$) undergoes a net energy shift of:

$$-1.93 \times 10^{-9} B - 5.79 \times 10^{-9} B = -7.72 \times 10^{-9} B \text{ eV}.$$

The shortest-wavelength line ($m_j = +1/2 \rightarrow -1/2$) undergoes a net energy shift of:

$$1.93 \times 10^{-9} B + 5.79 \times 10^{-9} B = 7.72 \times 10^{-9} B \text{ eV}.$$

The total energy difference between the two photons is:

$$\Delta E = -1.54 \times 10^{-8} B \text{ eV}.$$

Since $\lambda = c/f = hc/E$, we have $\Delta\lambda = -(hc/E^2)\Delta E = 0.022 \text{ nm}$, where $E = hc/\lambda$. Then, we can derive that $B = 0.51 \text{ T} = 5100 \text{ G}$, which is a typical value for photosphere magnetic field strength.

2.1.2 Doppler Velocity Measurements

Doppler velocity measurement of the solar atmosphere refers to investigating the motion of solar material by analyzing the shifts in the wavelength of spectrum emitted or absorbed by that material. These measurements are crucial for understanding various dynamic processes in the solar atmosphere, including solar winds, flares, and oscillations. Doppler velocity measurement method is a powerful tool for studying the 3-D velocity field of the solar atmosphere. For example, [Taro Morimoto & Hiroki Kurokawa \(2003\)](#) [10] developed a method to measure the 3-D velocity field of disappearing filaments. Their method consists of two steps: (1) the line-of-sight is obtained by calculating the H- α line profile of the filament and by measuring the Doppler shifts. The tangential velocity is obtained by tracing the motions of the structures.

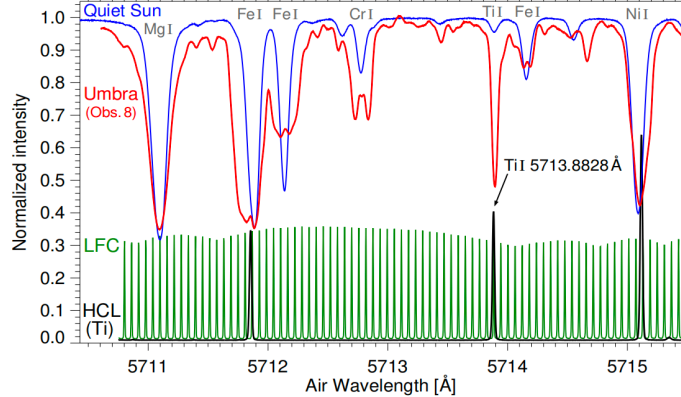


Figure 3: Spectra observed with LARS at around 5713 Å. The spectra were observed in the quiet Sun at disk center (blue), and in the sunspot umbra (red). The ions of the spectra lines are stated in gray color. The emission spectra of the laser frequency comb (LFC, green) and the titanium hollow cathode lamp (HCL, black) are also plotted for showing the calibration of absolute wavelengths and Doppler shifts. Figure directly adopted from [Löhner-Böttcher et al. \(2018\)](#) [9]

To illustrate how Doppler velocity measurement is used in solar physics, we take the work of [Löhner-Böttcher et al. \(2018\)](#) [9] as an example. The authors directly measured the Doppler velocities of the darkest part of sunspot umbrae with an unprecedented accuracy and precision using the Laser Absolute Reference Spectrograph (LARS) at the German Vacuum Tower Telescope. The spectral Ti I line at 5173.9 Å is selected since it becomes stronger in cooler atmosphere and returns no Zeeman effect due to the Landé g-factor of zero.

Figure 3 shows an overview of the spectra observation. To obtain a very good spectral precision, high resolution was essential. At a wavelength of $\lambda = 5714 \text{ Å}$ and a full width at half maximum

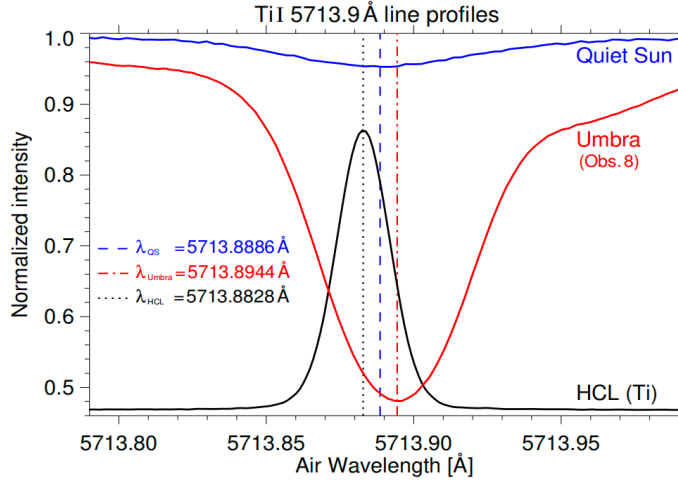


Figure 4: High-resolution observations of the Ti I 5713.9 Å line. The quiet Sun spectrum (blue) and umbral spectrum (red) are compared with the emission spectrum from the hollow cathode lamp (HCL, black). The center positions of fits to the line core are marked as blue dashed (quiet Sun), red dashed-dotted (umbra), and black dotted (HCL) lines. The corresponding wavelengths of the center positions are also marked on the left side of the plot. Figure directly adopted from [Löhner-Böttcher et al. \(2018\)](#) [9].

($\Delta\lambda \approx 8$ mÅ) of the instrumental profile, the authors obtain a resolution of $\lambda/\Delta\lambda > 700000$. A laser frequency comb served for the calibration of the spectrograph and the determination of the absolute wavelength scale of the solar spectrum. The solar spectrum and the frequency comb spectrum were recorded in an alternating order, enabling a quasi-simultaneous wavelength calibration.

A detailed view of the Ti I 5713.9 Å line is shown in Figure 4. To obtain a high precision of the measurement of the laboratory wavelength of the Ti I 5713.9 Å line, the authors used the hollow cathode lamp (HCL) as a reference. The good agreement between the line profile and a Voigt function yielded a central wavelength of $\lambda_0 = 5713.8828$ Å with an error of around 0.05 mÅ, which could be translated into an uncertainty of $\sigma_{\lambda_0} = 2.6$ m/s. With the laboratory wavelength λ_0 (or λ_{HCL}), it was possible to calculate the Doppler shift of the observed wavelength position λ of the solar spectral line. The line-of-sight Doppler velocity v_{los} was calculated by:

$$v_{los} = c \cdot (\lambda - \lambda_0) / \lambda_0 - v_{grs},$$

where c is the speed of light, $v_{grs} = +633$ km/s is the gravitational redshift (12.1 mÅ at $\lambda = 5713.9$ Å).

2.1.3 Profile Analysis

2.2 Typical Wavebands and Their Research Significance

Figure 5 is probably the best-known figure in solar physics, showing the average quiet Sun temperature distribution and the regions where various spectral features are formed. The spectra indicated are due to H , H^- , C , Si , Fe , $CaII$, and $MgII$. We have listed in Figure 6 the most common elements found in the Sun and the point of spectrum where the absorption/emission line is found, its width, features to be observed, and its height above the photosphere. In this section, we will introduce some typical wavebands that are often used to observe different layers of the solar atmosphere.

2.2.1 Photosphere

The Sun's *photosphere* is the out shell of the Sun from which light is radiated, appearing as a light, glowing surface. This layer is about 500 km thick and has a temperature ranging from 4500 to 6000 K. The photosphere is composed of convection cells called granules, which are about 1000 km in diameter and have a lifespan of about 8 to 20 minutes. The photosphere also exhibits sunspots,

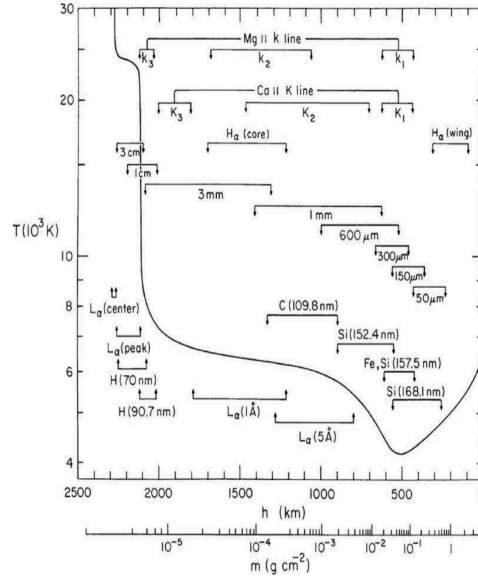


Figure 5: The average quiet-Sun temperature distribution derived from EUV continuum, and observations of different spectral lines. The approximate depths where the various continua and lines originate are indicated. Figure directly adopted from [Vernazza et al. \(1981\)](#) [16].

Wavelength (nm)	Name	Species	Equivalent width (nm) Disk Centre	Region	Height above Photosphere (Km)	Temp (K)
Soft X-rays				Corona	>5000	2,000,000
121.57	Lyman α	H		Upper chromosphere	2200	20,000
155		C IV		Transition region	2500	100,000
279.54	k	Mg II	2.2	UV emission, high chromosphere	500-1600	
280.23	h	Mg II	2.2			
388.36	(CN band head)	CN	0.03 (index)	Photosphere, magnetic field tracer		
393.36	K	Ca II	2	Chromosphere, flares, prominences	600-1500	
396.85	H	Ca II	1.5	Chromosphere, flares, prominences	1000-2000	
430.79	G band	CH (Fe I, Ti II)	0.72	Photosphere, flares, magnetic field tracer		
517.27	b2	Mg I	0.075	Low chromosphere		
518.36	b1	Mg I	0.025			
525.02		Fe I	0.007	Photosphere, magnetic fields (g=3)		
537.96		Fe I	0.0079	Medium photosphere		
538.03		C I	0.0025	Low photosphere		
557.61		Fe I		Photosphere, velocity fields (g=0)		
587.56	D3	He I		Chromosphere, flares, prominences		
589	D2	Na I	0.075	Upper photosphere, low chromosphere, prominences		
589.59	D1	Na I	0.056	Upper photosphere, low chromosphere, prominences		
612.22		Ca I		Photosphere, magnetic fields (g=1.5)		
630.25		Fe I	0.0083	Photosphere, magnetic fields (g=2.5)		
656.28	C (H α)	H I	0.41	Chromosphere, prominences, flares	1250-1700	
676.78		Ni I		Photosphere, oscillations		
769.89		K I		Photosphere, oscillations		
777.42		O I	0.0066	High photosphere		
849.8	Calcium 'infrared triplet'	Ca I	0.13	Low chromosphere, prominences		
854.21	Calcium 'infrared triplet'	Ca I	0.37	Low chromosphere, prominences		
866.2	Calcium 'infrared triplet'	Ca I	0.27	Low chromosphere, prominences		
868.86		Fe I	0.014	Photosphere, magnetic fields (g=1.7)		
1006.37		FeH		Umbral (only) magnetic fields (g=1.22)		
1083.03		He I	0.003	High chromosphere		
1281.81	H Paschb	H I	0.19	Chromosphere		
1564.85		Fe I	0.0035	Photosphere, magnetic fields (g=3)		
1565.29		Fe I	0.003	Photosphere, magnetic fields (g=1.8)		
2231.06		Ti I		Umbral (only) magnetic fields (g=2.5)		
4652.55	H Pfundb	H I		Chromosphere, electric fields		
4666.24		CO		High photosphere, thermal structure		
12318.3		Mg I		High photosphere, magnetic fields (g=1)		

Figure 6: The most common elements in the Sun and the wavelength (nm) where the absorption line is found within the spectrum, and the features to be observed.

which are cooler and darker regions caused by intense magnetic activity. A continuous spectrum, punctuated by absorption lines from a variety of elements, can be observed from the photosphere. The

spectrum reveals details of the Sun’s composition and physical conditions. In this section, we will go through some typical wavelengths that are often used to observe the photosphere and their research significance.

2.2.2 Chromosphere and Transition Region

The Sun’s *chromosphere* is a distinct layer above the photosphere and below the corona, extending about 2000 to 3000 kilometers. It is characterized by a reddish flow, best seen during solar eclipses, due to the emission of H- α light. Temperatures on the chromosphere increases with altitude, ranging from around 6000 K at the base to about 20,000 K at the top. This layer is also the site of spicules, which are dynamic and narrow jets of gas, and prominences, which are large, bright loops of plasma.

Above the chromosphere lies the *transition region*, which is a thin layer of the Sun’s atmosphere that separates the cooler chromosphere from the hotter corona. The temperature in the transition region rises rapidly from around 20,000 K to about 1 million K over a distance of a few hundred kilometers. Physical processes in the transition region are not well understood, but is believed to play a crucial role in the heating of the corona and the acceleration of the solar wind. The transition region emits strong ultraviolet radiation, showing rapid changes in temperature and density. In this section, we will introduce some typical wavelengths that are often used to observe the chromosphere and transition region. Their research significance will also be discussed.

Helium I D₃ The He I D₃ line (5876 Å) is generally formed in the upper chromosphere, and is sensitive to the local magnetic field. The He I D₃ line is also indirectly affected by the heating of the transition region and corona, since it is resulting from a transition that occurs between levels in the triplet system of neutral helium. These levels are generally populated via an ionization-recombination mechanism under the influence of EUV radiation originating in the transition region and corona ([Libbrecht 2019 \[7\]](#)). In Figure 7 we show raster scan of He I D₃ line in a flux emergence region. Since the He I D₃ line is usually weak on the solar disk, a continuum correction is necessary. This line also suffers from multiple telluric blends and some solar blends (see the right panel of Figure 7). [Libbrecht et al. \(2017\)](#) introduced a method to remove the telluric blends and presented their observations of Ellerman bombs with He I D₃ and He I 10830 Å lines.

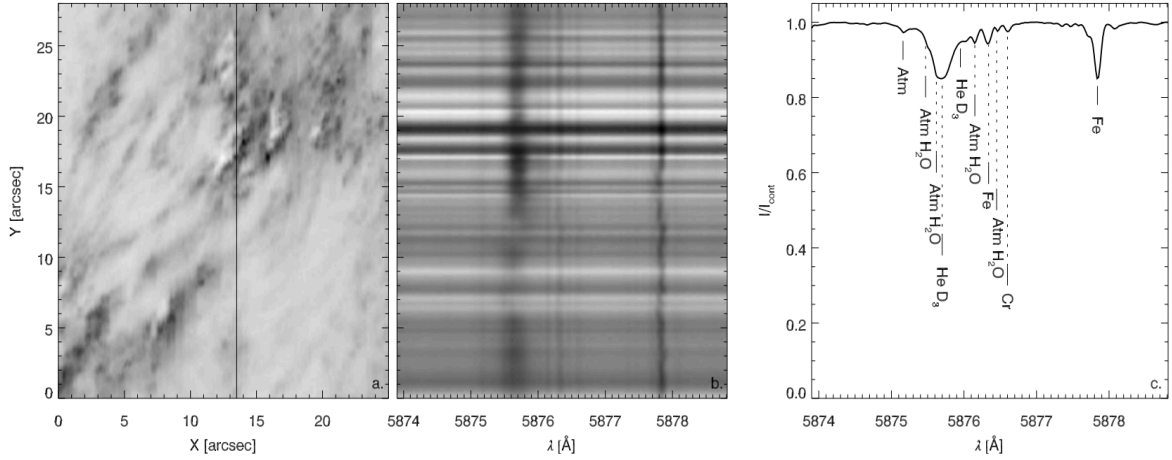


Figure 7: The He I D₃ line in a flux emergence region. The left panel shows the continuum-corrected line core raster scan at this wavelength, the middle panel shows the spectrum of He I D₃ corresponding to the vertical line on the left panel, the right panel presents the average spectrum as shown in the middle panel. Telluric lines are marked with ‘Atm’. Figure directly adopted from [Libbrecht \(2019\) \[7\]](#).

The He I D₃ line can be used to observe prominences and filaments. Prominences are large arcade-like structures which appear above the solar limb, while filaments are the on-disk features of prominences which appear dark against the continuum background. The prominence observation in He I D₃ is very weak (compared with H α observations), thus a proper scaling is needed if one wants to distinguish prominences from this line. Panels (a - c) of Figure 8 show an example of a prominence

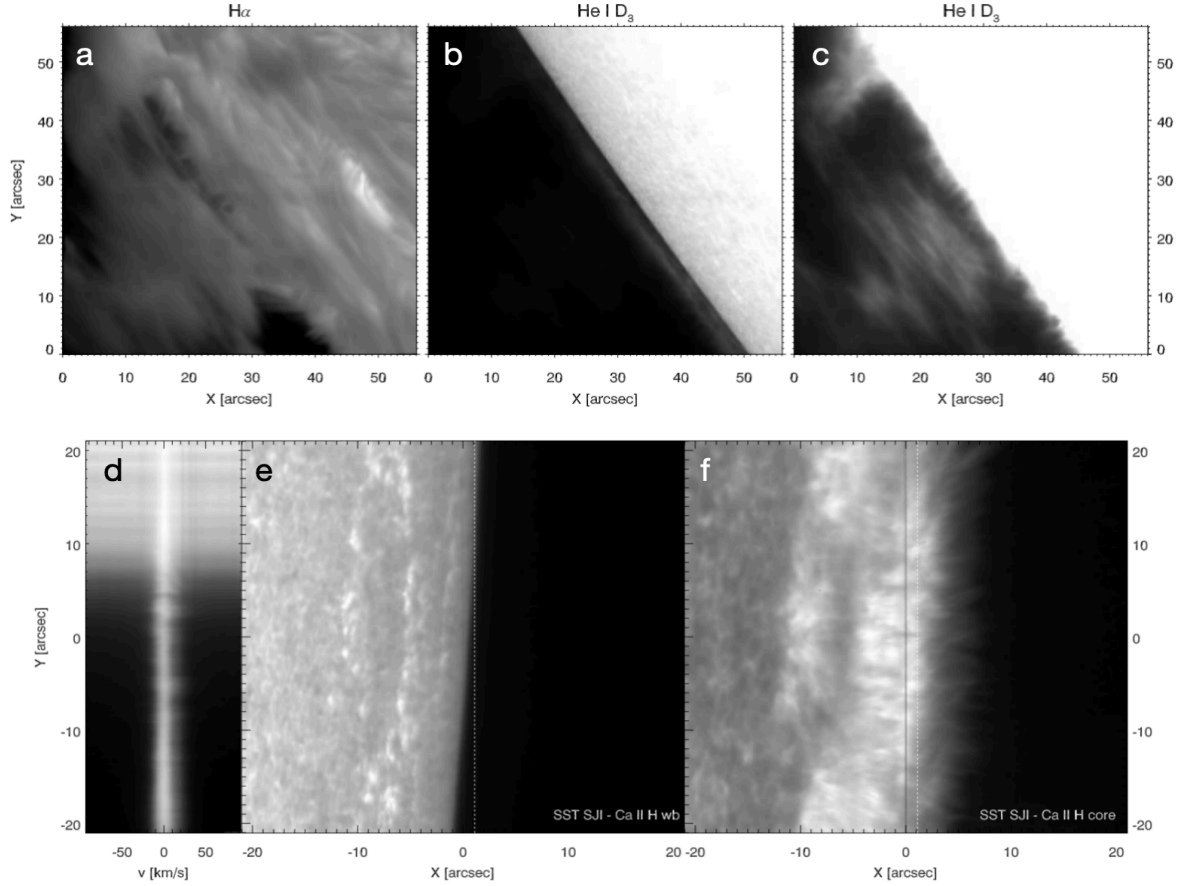


Figure 8: Prominence and Spicules observed in He I D₃ line. The first row shows prominence observed in H α (a), in He I D₃ (b), and in He I D₃ with proper scaling (c). The second row shows spicules observed in He I D₃ (left spectrum), slit-jaw images in Ca II H continuum (middle) and core (c).

as observed in the H α and He I D₃ wavebands. Spicules are thin tube-like chromospheric plasma structures which occur nearly everywhere on the Sun. They are capable of transporting mass and energy between photosphere and corona, and are believed to play an important role in coronal mass supply and heating (e.g., *De Pontieu et al. 2011*). An example of spicule observations in He I D₃ is given in panels (d - f) of Figure 8.

Many telescopes and instruments provide high-resolution observations of He I D₃. The Richard B. Dunn Solar Telescope (DST) is a 76 cm telescope located at Sacramento Peak in New Mexico. It is equipped with an He I D₃ prefilter, which allows it to take He I D₃ images with spectral tuning. The Swedish 1m Solar Telescope (SST, *Scharmer et al. 2003 [12]*) is located on the island of La Palma, Spain. It operates TRIPPEL, which is capable of observing three spectral regions simultaneously, meaning that He I 10830 Å and He I D₃ can be observed co-temperarily (e.g., *Libbrecht et al. 2017 [8]*). The spectral resolution of TRIPPEL is 200000, which promises the high-quality observations of He I D₃.

Calcium II H & K The Ca II H (3968.469 Å) and K (3933.663 Å) resonance lines was first employed to study fine structures in the solar chromosphere in the early work of *Jensen & Orrall (1963) [4]*, who elucidated aspects of the relationships between chromospheric K line structure and photospheric fine structure, and identified the oscillation nature of the K line variability. Figure 9 presents the absorption lines in the spectrum of Calcium II K and H showing the different regions where we should be observing the emission to see maximum line height details. As is seen, the central region of the K line is called K3 and the two smaller absorption regions are called K1. Each region shows a specific height of the chromosphere (see Figure 5). This is exactly mirrored in the H line. The two Calcium lines should be thought of as a doublet like the sodium doublet, with the only difference being how

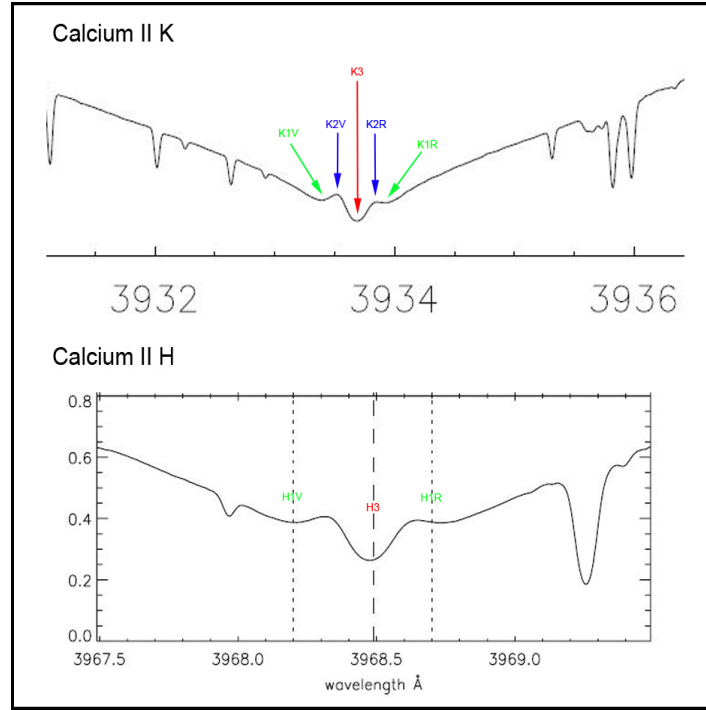


Figure 9: The regions of Ca II K and H line where different heights above the photosphere can be observed.

the transitions are made with the two outer shell electrons. Unlike other diagnostically important chromospheric lines such as Mg II h and k lines that reside in the ultraviolet part of the spectrum, the Ca II H and K lines are formed in the violet part of the visible spectrum and are thus more accessible to ground-based observations. Figure 10 shows the features that can be observed at the Ca II K line, including umbra and penumbra, bright ring, plages, and supergranulations. Umbra refers to the central dark region of sunspots, and penumbra refers to the lighter region surrounding the umbra. Within a developing active region (sunspot group) tiny spots form initially without a developed penumbra and are called pores. Active regions can contain either a single spot or a great number and can last from only a day up to 60 days. The bright ring is an area of brightening around penumbra. The discovery of the bright ring explains the missing energy due to suppression of convective energy transport by underlying magnetic fields. Chromospheric faculae can be observed anywhere on the solar disc and they are an extension of the photospheric faculae into the chromosphere. The supergranulation cells are large scale convective horizontal flow, where material flows outwards from the centre and downward flow has been observed at the boundaries. The flow carries both polarities to the boundaries ([Zirin 1988](#) [18]). K grains refer to the ‘intranetwork bright points’ found in the quiet sun. They originate from exclusively within cell interiors in quiet areas of the solar surface. Other phenomenon, such as Ellerman bombs and filaments, can also be observed at the Ca II K line, but appear more faint and less defined than in the H α window.

The H and K line wings are formed in the photosphere with their opacity following local thermal equilibrium (LTE) conditions ([Rutten et al. 2004](#) [11]). They were used to obtain the temperature stratification of the upper photosphere ([Roupe van der Voort 2002](#) [15]), and to investigate the granulation actions in both observation and simulation ([Leenaarts & Wedemeyer-Böhm 2005](#) [5]). The H and K line cores are formed in the chromosphere and cover a narrow spectral range of ~ 0.4 Å. Note that observations of H and K cores suffer from a strong contamination of the photospheric signal coming from the wings. The K line is also very sensitive to the magnetic field. If magnetic fields are present, absorption is less (more light is transmitted) with weaker magnetic fields showing as darker areas. Therefore, moderately strong magnetic field shows up as bright regions in our images but with the exception of very strong magnetic field, such as in a sunspot where they appear very dark.

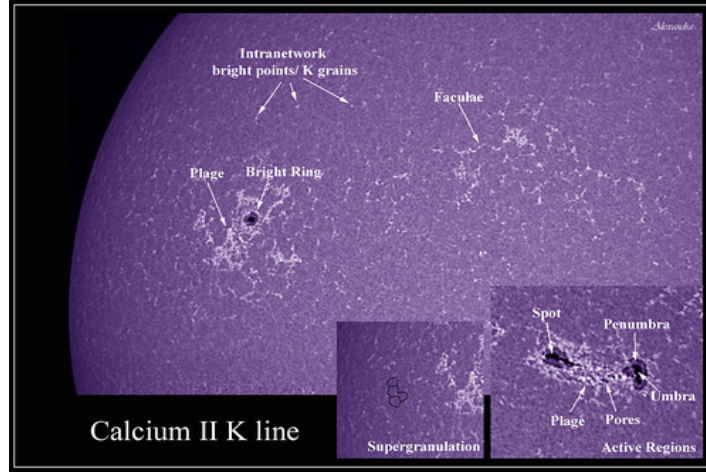


Figure 10: Features that can be observed at Ca II K line. The photograph is taken using a Coronado CaK PST telescope (40mm) and an Imaging Source DMK41 monochrome camera with false colour added.

Hydrogen alpha Hydrogen alpha (hereafter referred to as $H\alpha$) is a specific wavelength at 656.281 nm in the red part of the visible spectrum. A hydrogen atom emits or absorbs a photon at this wavelength when an electron transitions between the second energy level ($n=2$) and the third energy level ($n=3$). The $H\alpha$ line is one of the most popular lines for studying the chromosphere and its energetic events, such as filaments, Ellerman bombs, flares, and spicules (*Carlsson et al. 2019 [2]*). Figure 11 (a) shows the differences of the Sun in $H\alpha$ and white light. $H\alpha$ observations present more details of the chromosphere. Filaments appear as elongated dark structures against the solar disk (see Figure 11 (b)) in $H\alpha$ window. When viewed from the edge of the Sun against the dark background of space, filaments appear bright and glowing and are called prominences (see Figure 11 (c)). The brightness is a result of the emission of light by the cooler and denser plasma. Plages are bright and patchy regions in the chromosphere, which mark the sites of active regions and sunspot groups (see Figure 11 (d)). Weak flares, also known as Ellerman bombs or tiny micro-flares, also appear bright, making them easily be confused with plages. However, flares (see Figure 11 (e)) are unmistakable and involves a sudden brightening within a sunspot group often as multiple ribbons that resemble flows of white-hot lava. They can last from a few minutes to hours and change in both intensity and area. Figure 11 (f) shows spicules, which are jets of hot gas between 3,000 to 10,000 km high, seen in profile. They rim the solar circumference like "orange fur". These events leave spectral signatures in the $H\alpha$ intensity profiles, which can be used to investigate the fine-scale structure and temporal evolution of the chromosphere. For example, *Vissers et al. (2019) [17]* combined the observations from the Swedish 1-m Solar Telescope (SST) and the Atmospheric Imaging Assembly (AIA) on board the Solar Dynamics Observatory (SDO) at $H\alpha$ for developing a detection algorithm for Ellerman bombs.

Due to the complexity of the chromosphere, it is difficult to fully interpret the formation of the $H\alpha$ line in the chromosphere. On the one hand, the assumption of local thermodynamic equilibrium (LTE) is not always valid in the chromosphere. Non-LTE conditions mean that the population of energy levels in hydrogen atoms is influenced by the radiation field over a larger region, complicating the modeling of the $H\alpha$ line formation. On the other hand, radiative transfer through the chromosphere and the corona is extremely complex due to the non-LTE conditions and the 3D structures of the chromosphere. *Leenaarts et al. (2012) [6]* used advanced radiation-MHD simulations and 3D radiative transfer calculations to investigate the $H\alpha$ line formation in the chromosphere. They found that the $H\alpha$ line opacity is more sensitive to mass density than to temperature. This sensitivity implies that the $H\alpha$ line core intensity correlates with the average formation height: the higher the formation height, the lower the intensity. From the formation perspective, the reasons that make the $H\alpha$ line is such a good window to observe the Sun are: (1) it has so much opacity in its line core so that it always forms in the low plasma-beta region where the magnetic field dominates; (2) the low mass of the Hydrogen atom makes the line wide, so that the velocity field only has little influence on the fixed-wavelength line core intensity. Instead, it is the variation of the mass density caused by the magnetic field, waves,

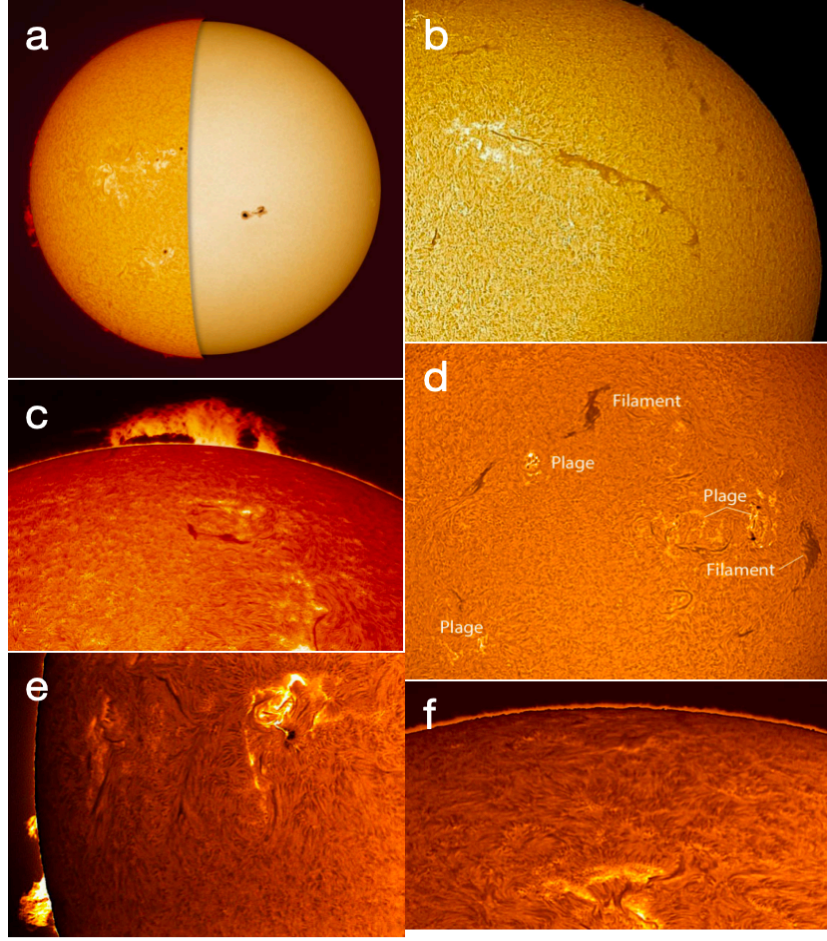


Figure 11: $H\alpha$ observations of the Sun, showing: (a) composite image of the Sun in $H\alpha$ (left) and white light (right), (b) a long filament, (c) a large quiescent prominence, (d) plages and filaments, (e) a C-class solar flare (upper right) and prominences (lower left), and (f) spicules.

and shocks that gives rise to the structures of the $H\alpha$ line. [Tarr et al. \(2019\)](#) [14] compared the Atacama Large Millimeter Array (ALMA) 3 mm emissions and $H\alpha$ solar observations, and confirmed that a strong correlation exists between the $H\alpha$ line width and the 3 mm brightness temperature. They also found a bimodal relation between the two diagnostics, with shallower slope in cooler regions and steeper slope in hotter regions. The origin of the bimodal distribution remains unknown, but does hold for the observations.

To observe the $H\alpha$ line with high spatial and spectral resolution, many efforts have been made by the solar physics community. High-resolution imaging spectroscopy in solar physics has relied on Fabry-Pérot interferometers (FPI) in recent years. For example, [Hu et al. \(2022\)](#) [3] introduced a tunable narrow-band imager with high spectral resolution based on a FPI they designed to observe the Sun at $H\alpha$ wavelength, and have shown the first results they obtained from the instrument plus a 65 cm solar telescope. The FPI has a bandpass (FWHM) of 0.09 Å and a free spectral range of 3.85 Å. However, FPI systems get technically challenging and expensive for telescopes larger than 1-m class. To overcome this, [Beck et al. \(2018\)](#) [1] introduced the design and utilization of the Interferometric Bidimensional Spectrometer (IBIS) for high-resolution solar observations. They use a subtractive double pass (SDP) technique, which enhances spectral and spatial resolution by passing the light through the interferometer twice, to capture the $H\alpha$ line. This method significantly reduces stray light and improves the contrast and clarity of the spectral lines.

2.2.3 Corona

The *Corona* is the outermost layer of the Sun’s atmosphere, extending around 10 solar radii from the Sun’s surface. It can be observed as a white halo surrounding the Sun during a solar eclipse. The corona is characterized by its extremely high temperature, ranging from 1 to 3 million K, which results in the emission of X-rays and ultraviolet radiation. The corona is composed of highly ionized gases, structured by the Sun’s magnetic field into loops, streamers, and plumes.

One of the most prominent features of the corona is its dynamic and complex nature, with intense changes driven by solar activities. *Coronal mass ejections (CMEs)* are large expulsions of plasma and magnetic field from the Sun’s corona, which could have profound effects on space weather. The corona also continuously emits the *solar wind*, a stream of charged particles that flows outward from the Sun, permeating the solar system and interacting with the Earth’s magnetosphere. Studying the corona is crucial for understanding solar-terrestrial interactions and predicting space weather phenomena. The *Parker Solar Probe* and the *Solar Orbiter* are two recent missions that aim to study the corona up close and provide new insights into the Sun’s outer atmosphere. In this section, we will discuss some typical wavelengths that are often used to observe the corona, and explain their importance in research.

3 Some Existing Solar Observatories and Their Performance

3.1 New Vacuum Solar Telescope (NVST)

3.2 GREGOR Solar Telescope

3.3 Solar Dynamics Observatory (SDO)

References

- [1] C Beck, R Rezaei, D Prasad Choudhary, S Gosain, A Tritschler, and RE Louis. High-resolution observations of $h\alpha$ spectra with a subtractive double pass. *Solar Physics*, 293(2):36, 2018.
- [2] Mats Carlsson, Bart De Pontieu, and Viggo H Hansteen. New view of the solar chromosphere. *Annual Review of Astronomy and Astrophysics*, 57(1):189–226, 2019.
- [3] Xingcheng Hu, Jinsheng Yang, Xuejun Rao, and Changhui Rao. Fabry–pérot interferometer-based tunable narrow-band imager for solar chromospheric observation: First results. *Solar Physics*, 297(6):74, 2022.
- [4] Eberhart Jensen and Frank Q Orrall. Observational study of macroscopic inhomogeneities in the solar atmosphere. iv. velocity and intensity fluctuations observed in the k line. *Astrophysical Journal*, vol. 138, p. 252, 138:252, 1963.
- [5] J Leenaarts and S Wedemeyer-Böhm. Dot tomography of the solar atmosphere-iii. observations and simulations of reversed granulation. *Astronomy & Astrophysics*, 431(2):687–692, 2005.
- [6] Jorrit Leenaarts, Mats Carlsson, and L Rouppe Van Der Voort. The formation of the $h\alpha$ line in the solar chromosphere. *The Astrophysical Journal*, 749(2):136, 2012.
- [7] Tine Libbrecht. *The diagnostic potential of the He I D3 spectral line in the solar atmosphere*. PhD thesis, Department of Astronomy, Stockholm University, 2019.
- [8] Tine Libbrecht, Jayant Joshi, Jaime de la Cruz Rodríguez, Jorrit Leenaarts, and Andrés Asensio Ramos. Observations of ellerman bomb emission features in he i d3 and he i 10 830 Å. *Astronomy & Astrophysics*, 598:A33, 2017.
- [9] J Löhner-Böttcher, W Schmidt, R Schlichenmaier, H-P Doerr, Tilo Steinmetz, and Ronald Holzwarth. Absolute velocity measurements in sunspot umbrae. *Astronomy & Astrophysics*, 617:A19, 2018.
- [10] Taro Morimoto and Hiroki Kurokawa. A Method for the Determination of 3-D Velocity Fields of Disappearing Solar Filaments. *Publications of the Astronomical Society of Japan*, 55(2):503–518, 04 2003.

- [11] RJ Rutten, RH Hammerschlag, FCM Bettonvil, P Sütterlin, and AG De Wijn. Dot tomography of the solar atmosphere-i. telescope summary and program definition. *Astronomy & Astrophysics*, 413(3):1183–1189, 2004.
- [12] Goran B Scharmer, Klas Bjelksjo, Tapio K Korhonen, Bo Lindberg, and Bertil Petterson. The 1-m swedish solar telescope. In *Innovative telescopes and instrumentation for solar astrophysics*, volume 4853, pages 341–350. SPIE, 2003.
- [13] PA Sturrock. Physics of the sun: Volume ii: The solar atmosphere. 2013.
- [14] Lucas A Tarr, Adam R Kobelski, Sarah A Jaeggli, Momchil Molnar, Gianna Cauzzi, and Kevin P Reardon. Spatio-temporal comparisons of the hydrogen-alpha line width and alma 3 mm brightness temperature in the weak solar network. *Frontiers in Astronomy and Space Sciences*, 9:978405, 2023.
- [15] LHM Rouppe van der Voort. Penumbral structure and kinematics from high-spatial-resolution observations of k. *Astronomy & Astrophysics*, 389(3):1020–1038, 2002.
- [16] Jorge E Vernazza, Eugene H Avrett, and Rudolf Loeser. Structure of the solar chromosphere. iii-models of the euV brightness components of the quiet-sun. *Astrophysical Journal Supplement Series*, vol. 45, Apr. 1981, p. 635-725., 45:635–725, 1981.
- [17] Gregal JM Vissers, Luc HM Rouppe van der Voort, and Robert J Rutten. Automating ellerman bomb detection in ultraviolet continua. *Astronomy & Astrophysics*, 626:A4, 2019.
- [18] Harold Zirin. Astrophysics of the sun. *Cambridge: University Press*, 1988.